The Effect of Topology in Lewis Pair Functionalized Metal Organic Frameworks on CO$_2$ Adsorption and Hydrogenation

Journal:	*Catalysis Science & Technology*
Manuscript ID	CY-ART-05-2018-001018.R1
Article Type:	Paper
Date Submitted by the Author:	30-Jul-2018
Complete List of Authors:	Ye, Jingyun; University of Minnesota Twin Cities, Chemistry Li, Lin; University of Pittsburgh, Chemical and Petroleum Engineering Johnson, Karl; University of Pittsburgh, Chemical and Petroleum Engineering

The Effect of Topology in Lewis Pair Functionalized Metal Organic Frameworks on CO₂ Adsorption and Hydrogenation

Jingyun Ye[*], Lin Li, and J. Karl Johnson[*]

Department of Chemical & Petroleum Engineering, University of Pittsburgh, Pittsburgh,

Pennsylvania 15261, United States

Abstract:

We have used density functional theory and classical grand canonical Monte Carlo simulations to identify two functionalized metal organic frameworks (MOFs) that have the potential to be used for both CO_2 capture from flue gas and catalytic conversion of CO_2 to valuable chemicals. These new materials based on MIL-140B and MIL-140C functionalized with Lewis pair (acid and base) moieties, which are integrated into the framework linkers. We show that the Lewis pair functional groups are capable of catalyzing heterolytic dissociation of H_2 and subsequent hydrogenation of CO_2 through concerted 2-H addition. We have examined the effect of pore size and framework topology on the competitive binding of H_2 and CO_2. We show that the small pore size of functionalized MIL-140B stabilizes the formation of a pre-activated CO_2 species and that this pre-activated CO_2 has a lower overall reaction barrier for hydrogenation of CO_2 to formic acid than a competing pathway in the same material that does not go through a pre-activated complex. We demonstrate that steric hindrance can potentially break energy scaling relationships, which limit the ability to optimize traditional heterogeneous catalysts, by independently changing one part of the CO_2 hydrogenation pathway, without negatively impacting other parts of the pathway. Specifically, we show that steric effects can reduce the CO_2 hydrogenation barrier without impacting the H_2 dissociation barrier or binding energy.

---

[*] Corresponding authors: jingyun.ye324@gmail.com and karlj@pitt.edu

1. Introduction

Capture of CO_2 from flue gas or the atmosphere coupled with catalytic hydrogenation of CO_2 into valuable chemicals and fuels has been identified as a way to reduce the net amount of CO_2 in the atmosphere.[1-6] One approach to increasing the economic viability of carbon capture and conversion is to design a single material that can be used for both the capture and catalytic conversion of CO_2, because such a material could increase efficiency through process intensification.[7] Metal organic frameworks (MOFs) are materials that have the potential to both capture[8-12] and catalytically convert[13, 14] CO_2. The use of MOFs in catalysis has attracted significant attention recently because of the potential to tailor the 3D architectural topology and modify the functionality of MOFs.[15-21] MOFs can be used to construct precisely designed single site catalysts with either metal free or metal complexes as catalytic active sites for a variety of different reactions.[16, 22-28] In previous work, we have used density functional theory (DFT) calculations to show that Lewis pair (LP) functional groups incorporated into MOFs can hydrogenate CO_2 to formic acid (FA) and ultimately to methanol.[29-32] The LP moieties heterolytically dissociate H_2 on the Lewis acid and base sites, producing hydridic and protic hydrogens, respectively. These hydrogens can be added to CO_2 in a concerted single step to produce FA. Consistent with Zimmerman et al.,[33] we found that the barriers for concerted 2H addition are generally lower than barriers for step-wise hydrogenation of CO_2 on typical heterogeneous metal catalysts.[34-37]

We have previously investigated functionalized UiO-66[29, 30] and UiO-67[31] for CO_2 hydrogenation. The UiO-6x family of MOFs have octahedral and tetrahedral cages, connected by narrow triangular windows. The window sizes are 0.6 and 0.8 nm, for UiO-66 and UiO-67, respectively.[38] In this paper we utilize MIL-140B and MIL-140C as platforms for creating

functionalized MOFs for CO_2 hydrogenation. MIL-140 is a class of porous zirconium dicarboxylate MOFs (MIL-140A, B, C, D) with triangular channels along the z axis, composed of Zr oxide chains connected with different dicarboxylate linkers.[39] These MOFs have higher chemical and thermal stability and hydrophobicity than UiO-66.[39] The small triangular pores of MIL-140A and 140B make these interesting for comparing and contrasting with UiO-6x. In addition, MIL-140 is readily functionalizable and the functionalized MOF can as stable as the pristine materials.[40, 41] In this work we consider MIL-140B and MIL-140C that have been functionalized with LP groups incorporated into the linkers, as shown in Figure 1. These functional groups are the same as used previously for UiO-67.[31] The Lewis base site is a N atom incorporated into one of the aromatic rings of the linker; the Lewis acid site is a BF_2 group bound to a carbon atom in the α position to N (see Figure 1b and 1d). These materials, having one functional group per unit cell, are denoted as MIL-140B-NBF_2 and MIL-140C-NBF_2.

In this work we examine the impact of pore size and topology of the MOF pores on the adsorption of CO_2 from a N_2/CO_2 mixture and the catalytic hydrogenation of CO_2 to FA. It has been shown that the topology of zeolites can strongly affect the catalytic activity and selectivity through confinement effects on transition states or intermediates.[42-46] It is reasonable to assume that similar effects will be seen for catalytically functionalized MOFs.
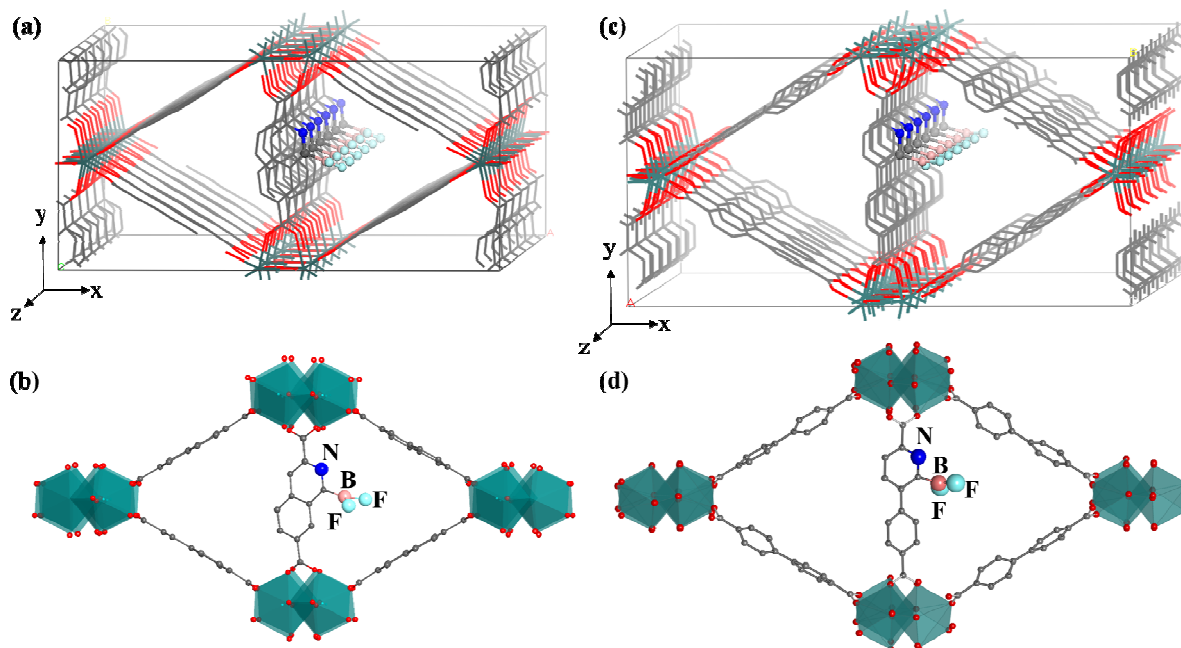
Figure 1. Structures of MIL-140B-NBF$_2$ and MIL-140C-NBF$_2$. Parts (a) and (c) illustrate the framework showing six unit cells along the z direction. The framework atoms are represented by lines, and the LP functional moieties are represented by balls and sticks. Colors of the atoms are as follows: pink for B, grey for C, dark blue for N, red for O, light blue for F, dark green for Zr. Parts (b) and (d) show unit cells of MIL-140B-NBF$_2$ and with MIL-140C-NBF$_2$ with Zr represented by polyhedral and the other atoms represented by balls and sticks. Hydrogen atoms are not shown for clarity.

2. Computational Details

All periodic DFT calculations were performed in the mixed Gaussian and plane wave approach implemented in the CP2K software package.[47] Van der Waals interactions were approximated with Grimme's D3 dispersion correction.[48] The Perdew–Burke–Ernzerhof (PBE) functional[49] was used to calculate the exchange-correlation energy. The DZVP-MOLOPT basis set was used in combination with Geodecker, Teter and Hutter pseudopotentials.[50] A plane wave cutoff energy of 360 Ry and a relative cutoff of 60 Ry were use in all calculations.

The unit cell of MIL-140B (see Figure S1a in the ESI[†]) was constructed from the data reported by Guillerm et al.[39] The fully relaxed lattice parameters are a = 28.24 Å, b = 13.46 Å, c = 7.85 Å, α = 90°, β = 93.43°, γ = 90°, which are in good agreement with experimental data,[39] as

4

seen from Table S1 of the ESI[†]. We fully relaxed the structure of MIL-140B-NBF$_2$ and obtained

lattice parameters: a = 28.22 Å, b = 13.44 Å, c = 7.85 Å, α = 90°, β = 93.43°, γ = 90°. We found

that the fully relaxed structure of MIL-140B-NBF$_2$ gave lattice constants that were almost

identical to that of the relaxed MIL-140B. Liang et al. found that functionalized analogues of

MIL-140 had lattice constants very similar to their parent structures,[40] which is consistent with

our findings. We therefore held the lattice constants fixed for further calculations of both MIL-

140B and MIL-140B-NBF$_2$. Our calculations for MIL-140C and MIL-140C- NBF$_2$ are reported

in Table S1 of the ESI[†]. The results for MIL-140C and its functionalized analogue are

qualitatively similar to our results for MIL-140B.

The adsorption of H$_2$ and CO$_2$ can be classified as either physisorption or chemisorption.

For physisorption H$_2$ and CO$_2$ are adsorbed molecularly and relatively weakly. Chemisorption of

H$_2$ is always dissociative with one H binding to the Lewis acid site and at Lewis base site.

Chemisorption of CO$_2$ is not dissociative, but is characterized by CO$_2$ bridging an LP site with

formation of C-N and O-B bonds.

The adsorption energy of H$_2$ or CO$_2$ is defined as:

$$E_{ad}(M) = E(M/MIL\text{-}140X\text{-}NBF_2) - E(MIL\text{-}140X\text{-}NBF_2) - E(M) \tag{0}$$

where M represents CO$_2$ or H$_2$, E(M/MIL-140X-NBF$_2$), E(MIL-140X-NBF$_2$) and E(M)

represents the total energy of MIL-140B-NBF$_2$ or MIL-140C-NBF$_2$ with the adsorbate, empty

MIL-140B-NBF$_2$ or MIL-140C-NBF$_2$, and the gas-phase molecule M, respectively. In the case

of co-adsorption, the adsorption energies were computed with respect to the sum of the total

energies of the corresponding gas-phase molecular species. According to the definition above,

negative values indicate that the process is exothermic and positive values are endothermic.

Transition states along the reaction pathway were determined by using the climbing image

nudged elastic band (CI-NEB) method[51] and were further confirmed through frequency analysis. Transition states were found to have a single imaginary frequency for a vibrational mode aligned with the reaction trajectory.

Grand canonical Monte Carlo (GCMC) simulations for adsorption of CO_2 and N_2 in MIL-140B/C and their functionalized analogues were performed with the RASPA simulation code[52] using the DREIDING force field[53] for the framework atoms. Charges on the framework atoms were computed for periodic cells using the DDEC method.[54, 55] The charges on the atoms of the unit cells are provided in the ESI[†]. We used the TraPPE models for N_2 and CO_2[56] and host-adsorbate interactions were computed from the Lorentz-Berthelot combining rules. 5×10^4 cycles were used for equilibration, followed by 1.5×10^6 cycles for data taking.

3. Results and Discussion

3.1 Trends in H_2 and CO_2 physisorption energies

We calculated the pore volumes of MIL-140B/C and MIL-140B/C-NBF$_2$ using PLATON.[57] The results are summarized in Table S2. Our calculated pore volume of MIL-140B is 0.23 cm^3g^{-1}, which is close to the reported pore volumes of 0.21 cm^3g^{-1} (simulated) and 0.18 cm^3g^{-1} (experimental).[39] The calculated density of MIL-140B is 1.43 g cm^{-3}, which is in good agreement with the reported value 1.55 g cm^{-3}.[39] The calculated pore volumes for our DFT optimized structures of MIL-140B/C-NBF$_2$ are very similar to the unfunctionalized counterparts. We have estimated physisorption energies for H_2 and CO_2 in MIL-140B and MIL-140B-NBF$_2$ by optimizing ten different geometries of H_2 and CO_2 in these materials from randomly generated initial configurations and computing binding energies within the PBE-D3 level of theory. The calculated physisorption energies of H_2 in MIL-140B are in the range of -0.16 ~ -0.23 eV. For CO_2 in MIL-140B the energies are in the range of -0.20 ~ -0.30 eV. The latter

values are close to the reported experimental isosteric heats of CO_2 adsorption about 0.27 eV.[40] Note that binding energies are approximately equal to the negative of isosteric heats.[58] The calculated physisorption energies of H_2 and CO_2 are in the range of -0.17 ~ -0.33 eV and -0.20 ~ -0.36 eV in MIL-140B-NBF_2, respectively. These results indicate that functionalization of MIL-140B with NBF_2 enhances the physisorption energies of H_2 and CO_2. We have also estimated the isosteric heats of adsorption from GCMC simulations using classical potentials. The isosteric heat for CO_2 at low loading (0.04 mmol/g) is 0.28 eV, in very good agreement with the experiments[40] and our DFT calculations. A plot of the isosteric heats for CO_2 in MIL-140B as a function of coverage calculated from our GCMC simulations are shown in Figure S2 of the ESI[†]. This gives us confidence that both our DFT-D3 calculations and GCMC simulations are able to capture the physisorption energetics correctly.

3.2 Adsorption isotherms and selectivities of CO_2 and N_2

As mentioned above, one advantage of using functionalized MOFs is that they hold the potential to be used both for separating CO_2 from flue gas and for catalytic reduction of CO_2. We have computed the adsorption isotherms from GCMC simulations for pure CO_2, pure N_2, and a 15 mol % mixture of CO_2 in N_2 at 298 K in functionalized and unfunctionalized MIL-140B/C. We modeled MOFs with one functionalized linker per pore, MIL-140B/C-NBF_2, and in the case of MIL-140B, four functionalized linkers per pore, MIL-140B-$(NBF_2)_4$. The isotherms computed from GCMC simulations are given in Figure S3 of the ESI[†]. Classical models, not accounting for chemisorption of CO_2 or N_2, were used in the simulations. The mixture isotherms were analyzed to estimate the selectivity of CO_2 over N_2, defined as $S_{CO_2/N_2} = \frac{y_{CO_2}}{y_{N_2}} \frac{x_{N_2}}{x_{CO_2}}$, where y_i and x_i are the mole fractions of i in the adsorbed and gas phases, respectively. The selectivities are plotted as a function of pressure in Figure 2. Our DFT calculations indicate that N_2 cannot chemisorb on

the LP sites (see Figure S4 of the ESI[†]), so inclusion of CO_2 chemisorption would only increase the selectivities reported in Figure 2. The values of S_{CO_2/N_2} increase in the order MIL-140C < MIL-140C-NBF$_2$ < MIL-140B < MIL-140B-NBF$_2$ < MIL-140B-(NBF$_2$)$_4$. We note that the DFT calculations presented below are performed on MIL-140B-NBF$_2$. However, our test calculations indicate that the number of NBF$_2$ groups per unit cell does not impact the DFT energies for chemisoption and reaction barriers, so we expect that all the results below apply equally as well for MIL-140B-(NBF$_2$)$_4$.
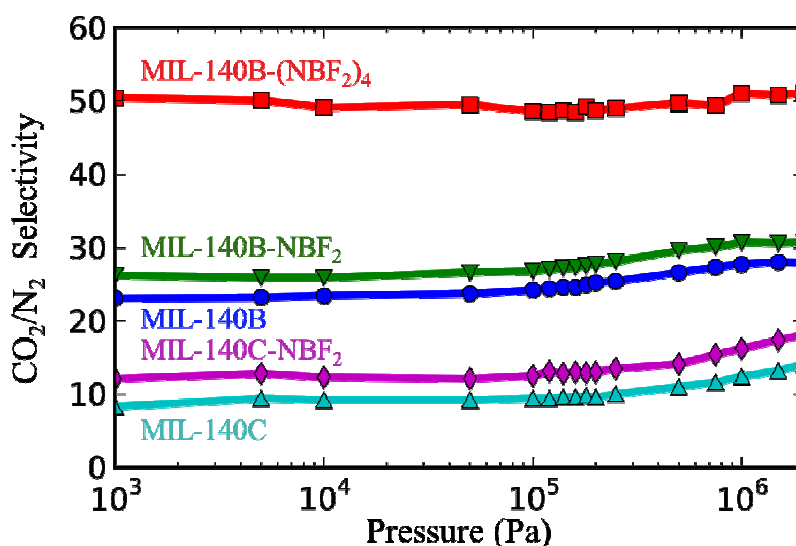
Figure 2. Selectivities of CO_2 over N_2 at 298 K as a function of pressure for (bottom to top) MIL-140C (light blue up triangles), MIL-140C-NBF$_2$ (purple diamonds), MIL-140B (blue circles), MIL-140B-NBF$_2$ (green down triangles) and MIL-140B-(NBF$_2$)$_4$ (red squares) as computed from GCMC simulations. The gas phase compositions were fixed at $y_{CO_2} = 0.15$ to mimic the concentration of CO_2 in flue gas.

3.3 Trends in H$_2$ and CO$_2$ chemisorption energies

Before focusing on the reaction pathways for CO_2 reduction, we first investigated the reactivity of the LP active sites towards the chemisorption of H_2 and CO_2. We do so by

comparing the dissociative adsorption energy of H_2 and chemisorption energy of CO_2 on the LP functionalized MIL-140B/C and UiO-66/67. These energies are plotted in Figure 3. The LP groups used in this work are comprised of N and BF_2 moieties linked via a C atom. The LPs are embedded in the ndc (2,6-naphthalenedicarboxylate) linker of MIL-140B or bpdc (biphenyl-4,40-dicarboxylate) linker of MIL-140C and UiO-67, as shown in Figure 1. The same LP sites are used in UiO-66-P-BF_2, but in this case the LP is part of a side chain connected to the linker, which is directed toward the center of the octahedral pore of UiO-66.[29-31] In this configuration, the LP in UiO-66-P-BF_2 has minimal steric interaction with the MOF framework. Note that the steric hindrance does not follow the order of pore size because of the placement of the LP group. The pore size increases in the order: MIL-140B (~8 Å)[40] < UiO-66 (~5 and ~9 Å)[59] < MIL-140C (~10 Å)[40] < UiO-67 (~12 Å and ~ 16 Å).[60]
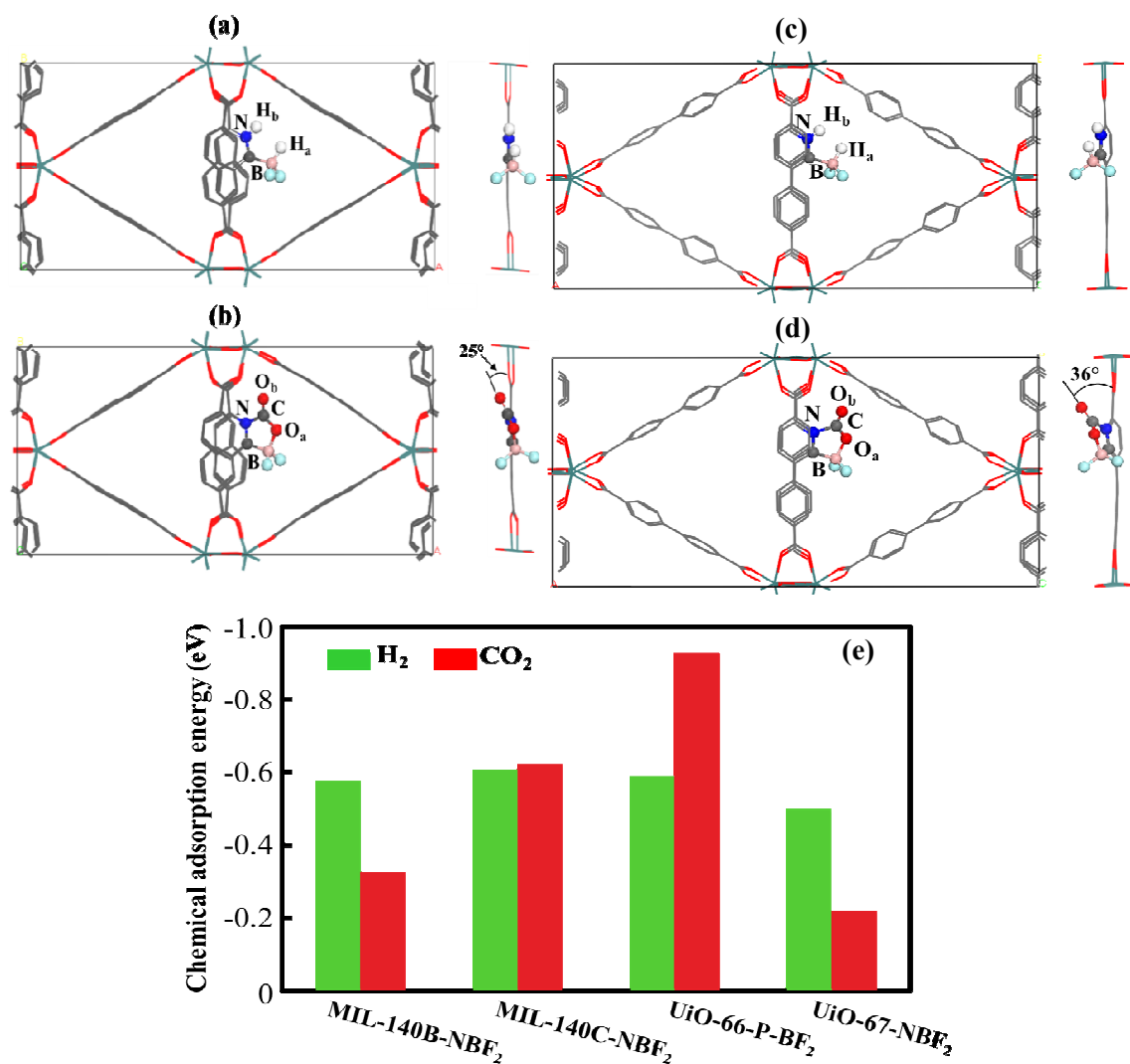
Figure 3. Optimized structures of chemisorbed H_2 (a) MIL-140B-NBF$_2$ and (c) MIL-140C-NBF$_2$. The structures of chemisorbed CO_2 in MIL-140B-NBF$_2$ and MIL-140C-NBF$_2$ are shown in (b) and (d), respectively. The side views are shown to the right of each of the unit cell front views. Part (e) presents the calculated chemical adsorption energies of H_2 and CO_2 on MIL-140B-NBF$_2$, MIL-140C-NBF$_2$, UiO-66-P-BF$_2$[29] and UiO-67-NBF$_2$.[31]

H_2 heterolytically dissociates with one H atom bound to B and another H atom bound to the N, generating hydridic (H_a) and protic (H_b) hydrogens, respectively, as shown in Figures 3a and 3c for MIL-140B-NBF$_2$ and MIL-140B-NBF$_2$, respectively. The calculated dissociative adsorption energy of H_2 is -0.63 eV in MIL-140B-NBF$_2$, and -0.61 eV in MIL-140C-NBF$_2$. These H_2 adsorption energies are extremely close to the value reported for UiO-66-P-BF$_2$ (-0.59

eV) and for UiO-67-NBF$_2$ (0.50 eV) without zero point energy corrections.[29, 31] These results

suggest that the effects of pore size and confinement do not significantly impact H$_2$

chemisorption. In contrast, CO$_2$ adsorption energies in these systems are significantly different.

The chemisorption energies of CO$_2$ on the incorporated NBF$_2$ moieties are -0.32 eV, -0.62 eV, -

0.93 eV and -0.22 eV on MIL-140B-NBF$_2$, MIL-140C-NBF$_2$, UiO-66-P-BF$_2$, and UiO-67-NBF$_2$,

respectively. The main reason that H$_2$ adsorption energies are nearly independent of pore size is

the small size of H$_2$; the chemisorbed H atoms do not exhibit steric hindrance with atoms in the

framework, as seen in Figures 3a and 3c. In contrast, the orientation of the bound CO$_2$ and

proximity of neighboring atoms explains why pore size and topology play a more important role

in the CO$_2$ binding to the LP.

Chemisorption of CO$_2$ results in a bent structure with one O atom (O$_a$) bound to B and

the C atom bound to N, as shown in Figures 3b and 3d and Figure S5 of the ESI†, for MIL-

140B/C-NBF$_2$ and UiO-67-NBF$_2$, respectively. Inside MIL-140B/C-NBF$_2$ and UiO-67-NBF$_2$,

the unbound O atom (O$_b$) points towards the O atoms of the carboxylate linkers (see Figure S6 of

the ESI†). The repulsion between these O atoms causes the adsorbed CO$_2$ to twist and become

non-coplanar with the linker. CO$_2$ twists by roughly 25° from the ndc linker for MIL-140B-NBF$_2$

(Figure 3b), 36° from the bpdc linker for MIL-140C-NBF$_2$ (Figure 3d) and 9° from the bpdc

linker for UiO-67-NBF$_2$ (Figure S5c, ESI†). The adsorption energy of CO$_2$ in MIL-140C-NBF$_2$ is

stronger than that in MIL-140B-NBF$_2$ because of the greater flexibility of bpdc linker of MIL-

140C, due to the topological differences in the linkers. The ndc linker of MIL-140B is composed

of fused rings, which are topologically more constrained than the bpdc linkers. This increase in

flexibility allows for a larger rotational degree of freedom in MIL-140C-NBF$_2$, in contrast to the

more rigid MIL-140B. For instance, the rotation of bpdc linkers is larger than that of ndc linkers,

and each phenyl ring of the bpdc linkers can also rotate independently, as shown in Figure 4a and

b. Additionally, the distance between the unbound O atom of CO_2 and the carboxylate O atoms

of nearby linkers is larger in MIL-140C than MIL-140B, as shown in Figure S6a and b. By

design, steric interaction is minimized in the UiO-66 system, because the LP functional group

points into the center of the pore. In UiO-66-P-BF$_2$, the bent CO_2 and the N and B atoms of the

LP are coplanar and CO_2 exhibits the strongest chemisorption[29] of the MOFs considered here.

Note that although UiO-67-NBF$_2$ has the largest pore, it has the smallest CO_2 chemisorption

energy (see Figure 3). This discrepancy may be explained by the strong repulsion between the

unbound O atom and the carboxylate O atoms on the nearby linkers. Specifically, CO_2 bound to

UiO-67-NBF$_2$ has the shortest O-O distance of any of the MOF studied here (see Figure S6 of

the ESI†). UiO-67 has 12 linkers per secondary building unit (SBU), which imposes a square

pyramidal vertex environment for the bound CO_2. This is a more confined environment than the

triangular prism edge that bound CO_2 experiences in MIL-140C, which has only 6 linkers per

SBU. Empty space exists between neighboring linkers that make up the sides of the triangular

prism in MIL-140C. The bound CO_2 molecule can therefore rotate and move the unbound O

atom towards this empty space in order to reduce the O-O repulsion. However, the gap between

nearby linkers is much smaller near the vertices in UiO-67. A rotation in this situation will

inevitably bring the unbound O atom closer to the carboxylate O on an adjacent linker. This

more constrained environment for UiO-67 is due to the different topology of the number of

linkers on the SBUs of UiO-67 and MIL-140C, and is the reason that CO_2 bound to UiO-67-

NBF$_2$ has the smallest twist angle, as discussed above.

(a)   (b)   (c)
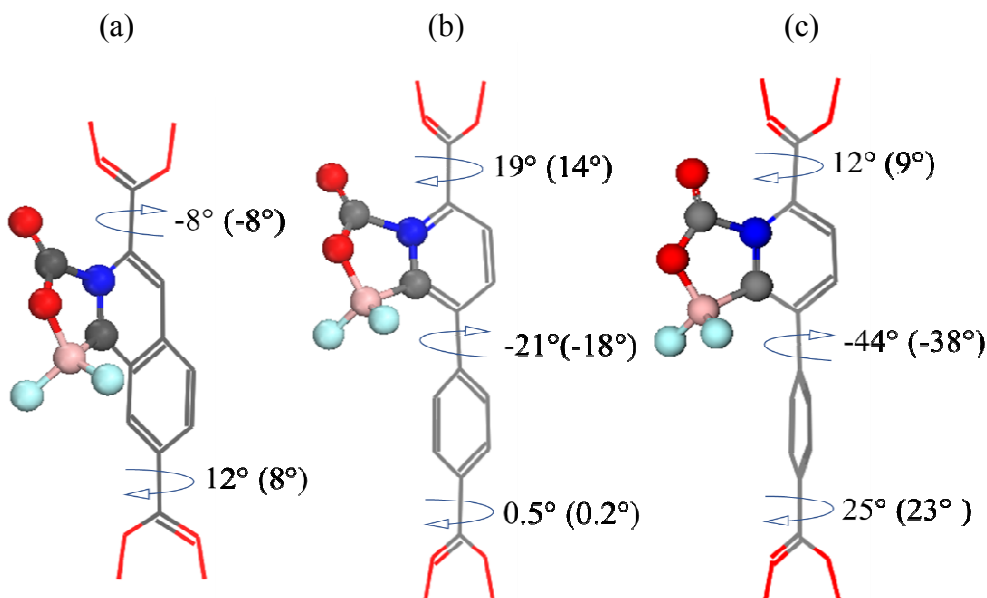
Figure 4. The torsion angles of the linkers of (a) MIL-140B-NBF$_2$, (b) MIL-140C-NBF$_2$ and (c) UiO-67-NBF$_2$ with chemisorbed CO_2. The values in the brackets are the torsion angles before the chemisorption of CO_2. The total change of the torsion angles after the chemisorption of CO_2 are 4°, 8° and 11° for MIL-140B-NBF$_2$, MIL-140C-NBF$_2$ and UiO-67-NBF$_2$, respectively.

3.4 CO_2 hydrogenation pathways in MIL-140B/C-NBF$_2$

We have seen how the effects of pore sizes and MOF topologies impact chemisorption of H_2 and CO_2. We now examine the impact of these same factors on hydrogenation of CO_2 by computing pathways and energy barriers for the concerted addition of two hydrogens to CO_2 to form FA in MIL-140B/C-NBF$_2$.

We identified two stationary starting configurations for CO_2 hydrogenation inside MIL-140B/C-NBF$_2$ with 2H*. One configuration is a linear CO_2, which is similar to the configurations observed in UiO-66-P-BF$_2$ and UiO-67-NBF$_2$.[29-31] The other configuration is a slightly bent CO_2, which exists due to confinement effects inside MIL-140B/C-NBF$_2$. We have calculated the energy barriers for hydrogenation of CO_2 to *cis*-FA starting from both linear and bent CO_2 inside the MOFs. The potential energy diagrams for CO_2 hydrogenation in MIL-140B/C-NBF$_2$ are plotted in Figure 5 and the structures of each state in the energy diagram for

MIL-140B/C-NBF$_2$ are shown in Figures S7-S10. In both MOFs, the bent CO$_2$ configuration is higher in energy than the linear configuration by ~0.4 eV. Additionally, the relative reaction barriers starting from bent CO$_2$ to FA are lower than starting from linear CO$_2$ in both MIL-140B/C-NBF$_2$. In MIL-140B-NBF$_2$, the hydrogenation barrier for going from a linear CO$_2$ to FA is 0.85 eV. This barrier is greatly reduced to 0.27 eV if the CO$_2$ is initially adsorbed in the bent geometry. In MIL-140C-NBF$_2$, the hydrogenation barrier is 0.65 eV for linear CO$_2$, and 0.33 eV for bent CO$_2$. Moreover, in MIL-140B-NBF$_2$, overall the transition state energy barrier starting from the linear and going through the bent CO$_2$ pathway is 0.7 eV, which is lower by 0.15 eV compared with starting from the same linear CO$_2$ configuration and going through another pathway that does not involve the bent intermediate. However, this is not true for MIL-140C-NBF$_2$, for which the overall transition state barrier starting from linear and going through the bent intermediate is 0.05 eV higher than the transition state obtained directly from the linear CO$_2$ structure (see Figure 5). We note that in each case the structures of the transition states obtained from the pre-activated bent CO$_2$ are slightly different from those obtained from starting from the linear CO$_2$. In the case of MIL-140B-NBF$_2$, the structure of the FA product is also slightly different (compare Figures S8 and S9 in the ESI†). For completeness we have computed the energetics of N$_2$ hydrogenation in hydrogenated MIL-140B-NBF$_2$. We found that the most favorable product state of the first step of N$_2$ hydrogenation is 2.5 eV higher in energy than the initial state (see Figure S4 in the ESI†). Therefore, we conclude that hydrogenation of N$_2$ is not likely to be feasible in LP functionalized MOFs.

We next focus on the origin of the pre-activation of CO$_2$ and consider how the bent CO$_2$ affects the barrier for hydrogenation of CO$_2$.
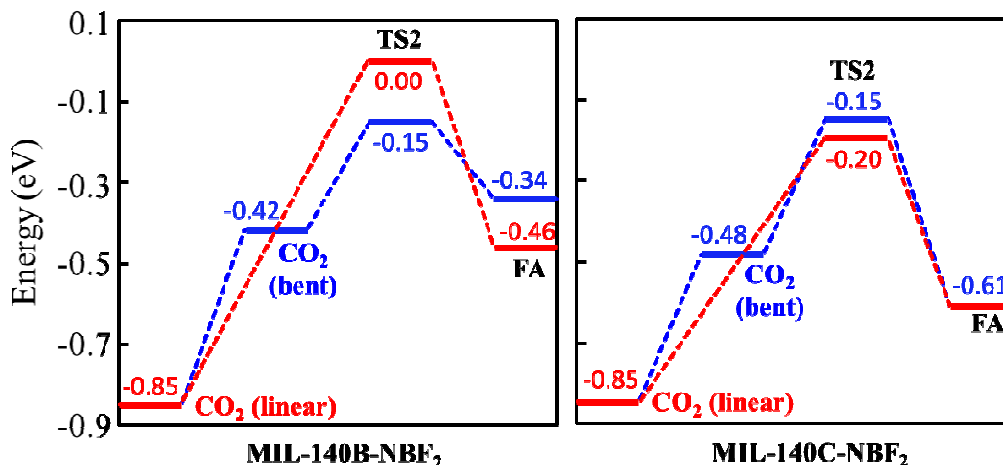
Figure 5. The energy diagrams for CO_2 hydrogenation from linear and bent configurations. The energy levels for CO_2 in the linear and bent states represent MIL-140B-NBF_2 and MIL-140C-NBF_2 having co-adsorbed CO_2 on the heterolytically split H_2 at the LP. FA represent energies associated with *cis*-formic acid vdW complexes near the LP inside the MOF, and TS2 represents the transition state for hydrogenation via concerted transfer of 2H* to CO_2. The zero of energy is CO_2, H_2 in the gas phase and the empty MOF.

3.5 Pre-activation of CO_2 for hydrogenation in MIL-140B-NBF_2

The potential energy profile shown in Figure 6 indicates that the diffusion of CO_2 from the linear to the bent configuration in MIL-140B-NBF_2 is endothermic and does not have an appreciable barrier in the reverse direction. In this study, we assumed the hydrogenation step follows an Eley-Rideal mechanism and the hydrogenation step is rate limiting. Under this premise, only three quantities: hydrogenation barrier, concentration of CO_2 in the pore, and the number of LPs with dissociated 2H* affect the overall reaction rate. Given the similar forms between the expression for the rate constant and the relative abundance of bent CO_2, one could combine these two quantities into an effective overall barrier.

Although the pre-activation step greatly reduces the hydrogenation reaction barrier, this improvement is counteracted by the fact that bent CO_2 is much less likely to be observed than linear CO_2. In the case of MIL-140B, pre-activating CO_2 netted a 0.15 eV improvement in the overall hydrogenation barrier. More importantly, confinement effects in MIL-140B resulted in a

15

much greater affinity for H_2 dissociation vs CO_2 chemisorption. This implies an even further improvement in the reaction rate due to having a greater number of LP sites with 2H* inside MIL-140B-NBF$_2$, relative to MIL-140C-NBF$_2$ and UiO-66-P-BF$_2$. Next, we discuss why CO_2 in the bent configuration is much more active toward hydrogenation.

The hydrogenation of CO_2 in a concerted mechanism occurs through nucleophilic hydride attack at the carbon site, coupled with electrophilic proton attack at the oxygen through the CO_2 frontier orbitals.[61] To understand how the geometry affects the electronic structure for reducing the hydrogenation barrier of bent CO_2, we analyzed the energies and shapes of the molecular orbitals of the bent and linear CO_2, together with the hydrogenated functionalized ligand. Molecular orbitals analysis was performed on the linear and bent CO_2 molecules in the gas phase by fixing their geometries in the linear and bent configurations taken from the optimized structures inside MIL-140B-NBF$_2$. For the orbital calculations of the cluster representation of MIL-140B-NBF$_2$(2H*), we fixed the geometry of the hydrogenated NBF$_2$ functionalized ligand and replaced the carboxylate groups with methyl groups, and the molecular orbital analysis was performed on the resulting cluster in the gas phase. As shown in Figure 6, the lowest unoccupied molecular orbital (LUMO) of the bent CO_2 protrudes out and exhibits strongly localized wave function probabilities, enhancing the interaction with the highest occupied molecular orbital (HOMO) localized at the nucleophiles (hydride H_a) by facilitating electron density transfer from the nucleophile (hydride H_a) into the LUMO of CO_2 molecule. In contrast, the LUMO of linear CO_2 shown in Figure 6, is symmetric, making transfer of an electron into that orbital less favorable compared with bent CO_2. Moreover, the gap between the HOMO of the hydrogenated LP and the LUMO of bent CO_2 is 0.98 eV smaller than for linear

CO_2. Hence, the lower barrier for bent CO_2 for hydrogenation can be ascribed to more favorable interactions of the frontier orbitals for bent CO_2 compared with linear CO_2.
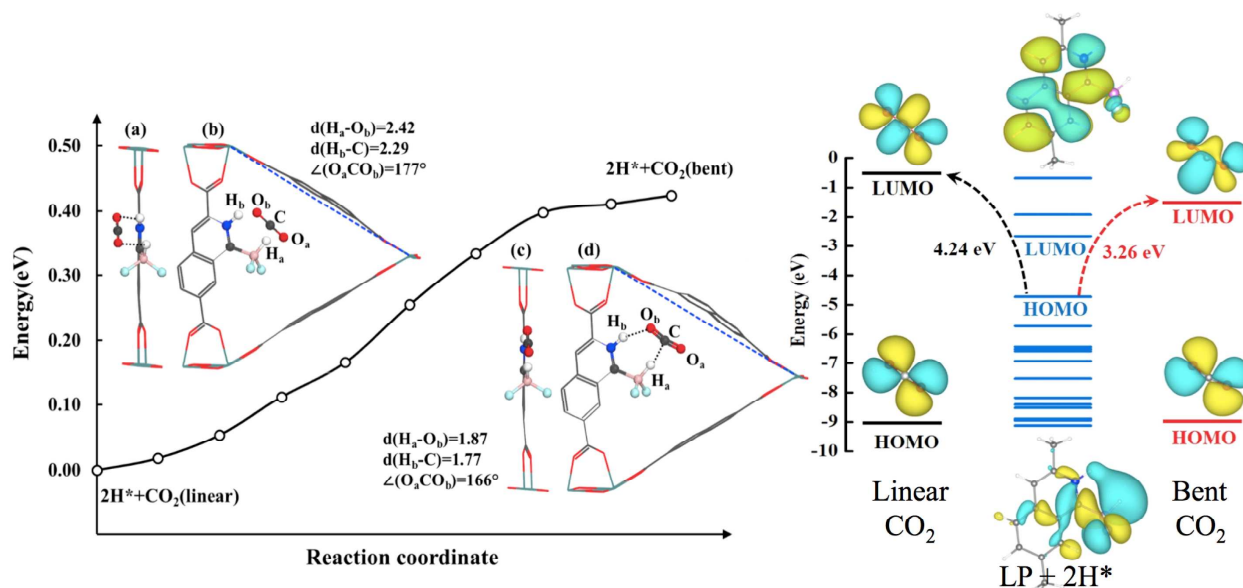
Figure 6. The left panel shows the CO_2 diffusion pathway from linear to bent configuration on MIL-140B-NBF$_2$. Parts (a) and (b) show the front and side view, respectively, of the LP with a linearly adsorbed CO_2. Parts (c) and (d) show the front and side view, respectively, of the LP with the CO_2 adsorbed in the bent state. The right panel show the HOMO-LUMO orbitals of the MIL-140B-NBF$_2$ ligand having dissociated 2H*, and linear and bent CO_2 molecules.

3.6 Effects of pore size on NBF$_2$ moiety for CO$_2$ hydrogenation

The potential energy diagrams for CO_2 hydrogenation on MIL-140B/C-NBF$_2$, UiO-66-P-BF$_2$ and UiO-67-NBF$_2$ shown in Figure 7. There are three energy barriers along the reaction pathway: H$_2$ dissociation, CO_2 hydrogenation, and FA desorption. We found that the reaction barrier for H$_2$ dissociation is 0.24 eV in MIL-140B-NBF$_2$ and 0.29 eV in MIL-140C-NBF$_2$ (See the structures in Figure S11 and S12 of the ESI[†]). Both have a much lower barrier than the same step in UiO-66-P-BF$_2$ (0.48 eV) and UiO-67-NBF$_2$ (0.46 eV). In all cases, the CO_2 hydrogenation step is rate limiting, and only the lowest overall effective hydrogenation barriers

in MIL-140B/C-NBF$_2$ were plotted, i.e., the effective barrier for the bent CO$_2$ pathway for MIL-140B-NBF$_2$ and the linear CO$_2$ pathway for MIL-140C-NBF$_2$. The relative energies for dissociative adsorption of H$_2$ and the co-adsorption of linear CO$_2$ on the 2H* appears to be the same (within about 0.04 eV) for MIL-140C-NBF$_2$ and MIL-140B-NBF$_2$. The barrier for the CO$_2$ hydrogenation step is 0.05 eV lower in MIL-140C-NBF$_2$, than in MIL-140B-NBF$_2$, and the resulting FA binds ~ 0.15 eV more strongly.

Although steric hindrance affects parts of the described CO$_2$ hydrogenation pathway, the resulting overall barrier for FA formation remained similar between MIL-140B-NBF$_2$ (0.70 eV), MIL-140C-NBF$_2$ (0.65 eV), and UiO-66-P-BF$_2$ (0.68 eV). It is important to note that this does not mean the overall reaction rate will be the same. One would expect MIL-140B-NBF$_2$ to be the most active out of the three, due to the fact that it is the only one that energetically prefers the dissociation of H$_2$ over the chemisorption of CO$_2$. The LPs on the MIL-140C-NBF$_2$ and UiO-66-P-BF$_2$ are expected to be passivated due to CO$_2$ poisoning. Thus, we have shown that it is possible to use confinement effects inside MOFs to improve the catalytic performance of the functional groups, not by directly changing the barrier of the rate-limiting step, but rather by tuning the selectivity of the LP functional groups toward H$_2$ dissociation relative to CO$_2$ chemisorption. Furthermore, we have demonstrated that steric effects are able to lower the CO$_2$ hydrogenation barrier without impacting the chemisorption of H$_2$, i.e., the pre-activated CO$_2$ pathway has a lower barrier for hydrogenation, even though the H$_2$ dissociation barrier and adsorption energy is unchanged. We have previously shown how the H$_2$ binding energy forms a scaling relationship with the CO$_2$ hydrogenation energy.[30] Decoupling elementary steps through pre-activation of CO$_2$ could be employed to break energy scaling relationships, which limit the design and performance of traditional heterogeneous catalysts. Including UiO-67-NBF$_2$ in the

comparison, we observe that this MOF has the lowest hydrogenation barrier (0.5 eV), is also resistant to CO_2 poisoning, but has the highest desorption barrier for FA (0.63 eV). Thus, it is desorption of FA that is the overall rate limiting step for UiO-67-NBF$_2$ and therefore MIL-140B-NBF$_2$ might still be the material that has the highest rate among the four MOFs considered here.
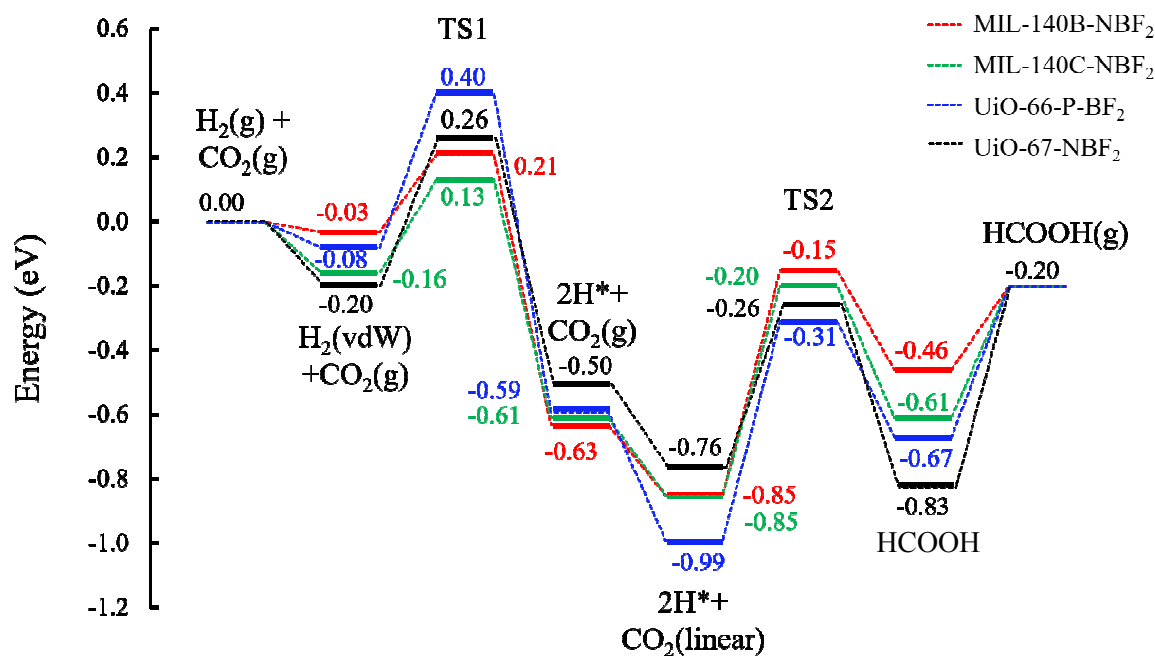
Figure 7. Potential energy profiles for CO_2 hydrogenation to formic acid in MIL-140B/C-NBF$_2$ and UiO-66-P-BF$_2$. TS1 represent the transition state for the heterolytic dissociation of H$_2$. TS2 represents the transition state that correspond to the lowest effective hydrogenation barrier in each MOF. Structures for the MIL-140B/C materials are given in Figures S7-S12 of the ESI[†].

4. Conclusion

The reaction pathways for the hydrogenation of CO_2 to FA in MIL-140B and MIL-140C functionalized with the NBF$_2$ were investigated using DFT calculations. The activities of CO_2 hydrogenation on these MOFs were compared with the activity on UiO-66-P-BF$_2$ and UiO-67-NBF$_2$. We have demonstrated that these MIL-140-based MOFs have high physisorption selectivity for CO_2 over N_2 and therefore have the potential to be used for both capture and

conversion of CO_2 from flue gas. We have compared the calculated chemisorption of H_2 and CO_2 in MIL-140B/C-NBF$_2$, UiO-66-P-BF$_2$ and UiO-67-NBF$_2$. We have found that the dissociative adsorption of H_2 is strongly favored over the chemisorption of CO_2 in MIL-140B-NBF$_2$ and UiO-67-NBF$_2$ in contrast to that in MIL-140C-NBF$_2$ and UiO-66-P-BF$_2$. This preference is due to confinement effects and topological constraints, and this finding demonstrates that one could vary the MOF topology to design MOF catalysts that could resist CO_2 poisoning.

Additionally, confinement effects in the MIL-140B/C also revealed a strategy to improve catalyst performance by pre-activating CO_2 via a bent physisorbed configuration. The barrier for CO_2 hydrogenation in MIL-140B/C-NBF$_2$ decreased by the formation of bent CO_2 co-adsorption with dissociated hydrogen atoms because the decrease of the energy level of LUMO of the bent CO_2 facilitates electron transfer from the HOMO of H atoms bound to the Lewis pair. However, this improvement is partially offset by the fact that CO_2 in the bent state is in a higher energy configuration. This resulted in an overall small but significant difference in the effective hydrogenation barrier between the pre-activated and linear pathways. Thus, the biggest increase in the reaction rate in our study would likely come from the improved selectivity of H_2 over CO_2 on the LP.

In summary, our study has shown that pore-confinement effects together with the steric hindrance of the functional group in functionalized MOFs could be used to improve catalysts design in two primary ways. First, the pre-activation of CO_2 can improve the hydrogenation barrier; if a more energetically favorable pathway to pre-activation could be found then the reduction in the barrier could be substantial. Therefore, finding a better method to achieve a pre-activation of CO_2 is crucial to significantly improving reaction rates. The second approach

focuses on improving the selectivity of the active site. Here, we have demonstrated that steric effects were able to specifically decrease the reactivity of the LP towards CO_2 without affecting rest of the CO_2 hydrogenation pathways.

[†]**Electronic supplementary information (ESI) available:** Lattice constants, atomic charges, isosteric heats, structural information, and potential energy diagrams.

Acknowledgments

References

1. G. A. Olah, G. S. Prakash and A. Goeppert, *J. Am. Chem. Soc.*, 2011, **133**, 12881-12898.
2. A. Dibenedetto, A. Angelini and P. Stufano, *J. Chem. Technol. Biotechnol.*, 2014, **89**, 334-353.
3. Y. Izumi, *Coord. Chem. Rev.*, 2013, **257**, 171-186.
4. R. J. Lim, M. Xie, M. A. Sk, J.-M. Lee, A. Fisher, X. Wang and K. H. Lim, *Catal. Today*, 2014, **233**, 169-180.
5. J. Ma, N. Sun, X. Zhang, N. Zhao, F. Xiao, W. Wei and Y. Sun, *Catal. Today*, 2009, **148**, 221-231.
6. J. Qiao, Y. Liu, F. Hong and J. Zhang, *Chem. Soc. Rev.*, 2014, **43**, 631-675.
7. A. Stankiewicz and J. A. Moulijn, *Industrial & Engineering Chemistry Research*, 2002, **41**, 1920-1924.
8. E. S. Sanz-Pérez, C. R. Murdock, S. A. Didas and C. W. Jones, *Chem. Rev.*, 2016, **116**, 11840-11876.
9. Y. Belmabkhout, V. Guillerm and M. Eddaoudi, *Chem. Eng. J.*, 2016, **296**, 386-397.
10. R. Sabouni, H. Kazemian and S. Rohani, *Environmental Science and Pollution Research*, 2014, **21**, 5427-5449.
11. A. Samanta, A. Zhao, G. K. H. Shimizu, P. Sarkar and R. Gupta, *Industrial & Engineering Chemistry Research*, 2012, **51**, 1438-1463.
12. J.-R. Li, Y. Ma, M. C. McCarthy, J. Sculley, J. Yu, H.-K. Jeong, P. B. Balbuena and H.-C. Zhou, *Coord. Chem. Rev.*, 2011, **255**, 1791-1823.
13. H. Fei, M. D. Sampson, Y. Lee, C. P. Kubiak and S. M. Cohen, *Inorg. Chem.*, 2015, **54**, 6821-6828.
14. Y. Lee, S. Kim, J. K. Kang and S. M. Cohen, *Chem. Commun.*, 2015, **51**, 5735-5738.
15. D. Farrusseng, S. Aguado and C. Pinel, *Angew. Chem. Int. Ed.*, 2009, **48**, 7502-7513.
16. L. Ma, C. Abney and W. Lin, *Chem. Soc. Rev.*, 2009, **38**, 1248-1256.
17. J. Liu, L. Chen, H. Cui, J. Zhang, L. Zhang and C.-Y. Su, *Chem. Soc. Rev.*, 2014, **43**, 6011-6061.
18. J. M. Falkowski, T. Sawano, T. Zhang, G. Tsun, Y. Chen, J. V. Lockard and W. Lin, *J. Am. Chem. Soc.*, 2014, **136**, 5213-5216.
19. D. Zhao, D. J. Timmons, D. Yuan and H.-C. Zhou, *Acc. Chem. Res.*, 2011, **44**, 123-133.
20. T. Zhang and W. Lin, *Chem. Soc. Rev.*, 2014, **43**, 5982-5993.
21. A. Aijaz and Q. Xu, *J. Phys. Chem. Lett.*, 2014, **5**, 1400-1411.
22. A. Herbst, A. Khutia and C. Janiak, *Inorg. Chem.*, 2014, **53**, 7319-7333.
23. L. Ma, M. M. Wanderley and W. Lin, *ACS Catal.*, 2011, **1**, 691-697.
24. F. Vermoortele, R. Ameloot, A. Vimont, C. Serre and D. De Vos, *Chem. Commun.*, 2011, **47**, 1521-1523.
25. X.-B. Han, Z.-M. Zhang, T. Zhang, Y.-G. Li, W. Lin, W. You, Z.-M. Su and E.-B. Wang, *J. Am. Chem. Soc.*, 2014, **136**, 5359-5366.
26. C. Wang, J.-L. Wang and W. Lin, *J. Am. Chem. Soc.*, 2012, **134**, 19895-19908.
27. J. Yang, P. Li and L. Wang, *Catal. Commun.*, 2012, **27**, 58-62.
28. X. Zhang, F. X. Llabrés i Xamena and A. Corma, *J. Catal.*, 2009, **265**, 155-160.
29. J. Ye and J. K. Johnson, *ACS Catal.*, 2015, **5**, 2921-2928.
30. J. Ye and J. K. Johnson, *ACS Catal.*, 2015, **5**, 6219-6229.
31. J. Ye and J. K. Johnson, *Catal. Sci. Technol.*, 2016, **6**, 8392-8405.
32. J. Ye, B. Y. Yeh, R. A. Reynolds and J. K. Johnson, *Mol. Simul.*, 2017, DOI: 10.1080/08927022.2017.1295457, 1-7.
33. P. M. Zimmerman, Z. Zhang and C. B. Musgrave, *Inorg. Chem.*, 2010, **49**, 8724-8728.
34. J. Ye, C.-j. Liu, D. Mei and Q. Ge, *J. Catal.*, 2014, **317**, 44-53.
35. J. Ye, C. Liu and Q. Ge, *J. Phys. Chem. C*, 2012, **116**, 7817-7825.

36.   G. Peng, S. J. Sibener, G. C. Schatz and M. Mavrikakis, *Surf. Sci.*, 2012, **606**, 1050-1055.
37.   G. Peng, S. J. Sibener, G. C. Schatz, S. T. Ceyer and M. Mavrikakis, *J. Phys. Chem. C*, 2012, **116**, 3001-3006.
38.   J. H. Cavka, S. Jakobsen, U. Olsbye, N. Guillou, C. Lamberti, S. Bordiga and K. P. Lillerud, *J. Am. Chem. Soc.*, 2008, **130**, 13850-13851.
39.   V. Guillerm, F. Ragon, M. Dan-Hardi, T. Devic, M. Vishnuvarthan, B. Campo, A. Vimont, G. Clet, Q. Yang, G. Maurin, G. Férey, A. Vittadini, S. Gross and C. Serre, *Angew. Chem. Int. Ed.*, 2012, **51**, 9267-9271.
40.   W. Liang, R. Babarao, T. L. Church and D. M. D'Alessandro, *Chem. Commun.*, 2015, **51**, 11286-11289.
41.   W. Liang, R. Babarao and D. M. D'Alessandro, *Inorg. Chem.*, 2013, **52**, 12878-12880.
42.   R. Gounder and E. Iglesia, *Acc. Chem. Res.*, 2012, **45**, 229-238.
43.   A. Bhan and E. Iglesia, *Acc. Chem. Res.*, 2008, **41**, 559-567.
44.   M. N. Mazar, S. Al-Hashimi, A. Bhan and M. Cococcioni, *J. Phys. Chem. C*, 2012, **116**, 19385-19395.
45.   A. J. Jones, S. I. Zones and E. Iglesia, *J. Phys. Chem. C*, 2014, **118**, 17787-17800.
46.   D. A. Simonetti, R. T. Carr and E. Iglesia, *J. Catal.*, 2012, **285**, 19-30.
47.   J. VandeVondele, M. Krack, F. Mohamed, M. Parrinello, T. Chassaing and J. Hutter, *Comput. Phys. Commun.*, 2005, **167**, 103-128.
48.   S. Grimme, J. Antony, S. Ehrlich and H. Krieg, *J. Chem. Phys.*, 2010, **132**, 154104.
49.   J. P. Perdew, K. Burke and M. Ernzerhof, *Phys. Rev. Lett.*, 1996, **77**, 3865-3868.
50.   S. Goedecker, M. Teter and J. Hutter, *Phys. Rev. B*, 1996, **54**, 1703-1710.
51.   G. Henkelman, B. P. Uberuaga and H. Jónsson, *J. Chem. Phys.*, 2000, **113**, 9901-9904.
52.   D. Dubbeldam, S. Calero, D. E. Ellis and R. Q. Snurr, *Mol. Simul.*, 2016, **42**, 81-101.
53.   S. L. Mayo, B. D. Olafson and W. A. Goddard, *The Journal of Physical Chemistry*, 1990, **94**, 8897-8909.
54.   T. A. Manz and D. S. Sholl, *J. Chem. Theory Comput.*, 2010, **6**, 2455-2468.
55.   T. A. Manz and D. S. Sholl, *J. Chem. Theory Comput.*, 2012, **8**, 2844-2867.
56.   J. J. Potoff and J. I. Siepmann, *AIChE J.*, 2001, **47**, 1676-1682.
57.   A. Spek, *J. Appl. Crystallogr.*, 2003, **36**, 7-13.
58.   S. E. Weber, S. Talapatra, C. Journet, A. Zambano and A. D. Migone, *Phys. Rev. B*, 2000, **61**, 13150-13154.
59.   C. Hon Lau, R. Babarao and M. R. Hill, *Chem. Commun.*, 2013, **49**, 3634-3636.
60.   X. Zhu, B. Li, J. Yang, Y. Li, W. Zhao, J. Shi and J. Gu, *ACS Applied Materials & Interfaces*, 2015, **7**, 223-231.
61.   A. M. Appel, J. E. Bercaw, A. B. Bocarsly, H. Dobbek, D. L. DuBois, M. Dupuis, J. G. Ferry, E. Fujita, R. Hille, P. J. A. Kenis, C. A. Kerfeld, R. H. Morris, C. H. F. Peden, A. R. Portis, S. W. Ragsdale, T. B. Rauchfuss, J. N. H. Reek, L. C. Seefeldt, R. K. Thauer and G. L. Waldrop, *Chem. Rev.*, 2013, **113**, 6621-6658.

TOC Graphic

MIL-140B-NBF$_2$

H$_2$+CO$_2$

HCOOH